



# Two-dimensional numerical simulations of vortex-induced vibrations for wind turbine towers

Axelle Viré<sup>1</sup>, Adriaan Derksen<sup>1,2</sup>, Mikko Folkersma<sup>1</sup>, and Kumayl Sarwar<sup>2</sup>

<sup>1</sup>Wind Energy Section, Faculty of Aerospace Engineering, Delft University of Technology, The Netherlands

<sup>2</sup>Siemens Gamesa Renewable Energy, Den Haag, The Netherlands

**Correspondence:** Axelle Viré (a.c.vire@tudelft.nl)

## Abstract.

Vortex-induced vibrations (VIV) of wind turbine towers can be critical during the installation phase, when the rotor-nacelle assembly is not yet mounted on the tower. The present work uses numerical simulations to study VIV of a two-dimensional cylinder under conditions that are representative of wind turbine towers, both from a fluid-dynamics and structural-dynamics perspective. First, the numerical tools and fluid-structure interaction algorithm are verified by considering a cylinder vibrating freely in a laminar flow. In that case, both the motion amplitude and frequency are shown to agree well with previous results from the literature. Second, VIV is modelled in the turbulent supercritical regime using Unsteady Reynolds-Averaged Navier–Stokes equations. In this context, the turbulence model is first validated on flow past a stationary cylinder at high Reynolds number. Then, results from forced vibrations are validated against experimental results for a range of reduced frequencies and velocities. It is shown that the behaviour of the aerodynamic damping changes with the frequency ratio, and can therefore lead to either self-limiting or self-exciting VIV when the cylinder is left to freely vibrate. Finally, results are shown for a freely-vibrating cylinder under realistic flow and structural conditions. While a clear lock-in map is identified and shows good agreement with published numerical and experimental data, the work also highlights the unsteady nature of the aerodynamic forces and motion under certain operating conditions.

## 1 Introduction

Vortex-induced vibrations (VIV) are structural vibrations that can occur due to the shedding of flow vortices when a fluid flow passes around a structure. Due to this fluid-structure interaction (FSI) phenomenon, a synchronization (also called lock-in) of the vortex shedding and the structural motion can occur for certain flow conditions and/or structural properties, leading to premature fatigue failures. Vortex-induced vibrations occur in many engineering applications, such as suspension bridges, marine risers, and industrial chimneys. In the context of wind energy, such vibrations have been observed both on the tower (Livanos, 2018; Derksen, 2019) and the wind turbine rotor (Heinz et al., 2016; Horcas et al., 2019). The increase in rotor height and diameter makes VIV an increasingly problematic issue when designing the new generation of wind turbines. This work is motivated by the specific problem of VIV of wind turbine towers during their installation. In that phase, when the tower does not yet support the rotor-nacelle assembly, it acts as a beam clamped at one of its ends and subjected to a wind flow. Because of



25 the vortex shedding developing in the tower wake, the tower may start to oscillate. This is particularly critical at three different stages of the installation process, namely when the tower: (i) stands on the quay-side, (ii) is transported on a vessel offshore, and (iii) is installed on the offshore foundation in the absence of rotor-nacelle assembly.

Although wind turbine towers are tapered, they resemble a circular cylinder. The phenomenological aspects of VIV for circular cylinders have been extensively analysed in the literature since several decades. However, studies at large Reynolds numbers and large mass ratios (defined as the ratio between the structure mass and the mass of the displaced fluid) are still quite rare. Experiments in both air (Feng, 1968; Brika and Laneville, 1993) and water (Govardghan and Williamson, 2000) showed that cylinders with large mass ratios exhibit much smaller amplitudes of vibrations than those with low mass ratios. Belloli et al. (2012) however showed that this is not necessarily true under large Reynolds numbers of the order of  $Re = 50,000$ . In this context, the maximum non-dimensional oscillation amplitude can become larger than the cylinder diameter. This was also described in other studies with low mass ratios (Govardghan and Williamson, 2006). For this reason, the original Griffin plot (Griffin, 1980), describing the maximum oscillation amplitude as a function of the mass damping parameter, needs to be modified for large Reynolds numbers.

It is worth noting that all these VIV studies were limited to the subcritical regime, in which the boundary layer remains fully laminar and the drag coefficient is nearly constant with the Reynolds number. By contrast, wind turbine towers experience flows both in the transitional regime ( $1.5 \cdot 10^5 \leq Re \leq 3.5 \cdot 10^6$ ), where laminar separation bubbles can exist and reduce the drag coefficient, and in the supercritical regime ( $Re \geq 3.6 \cdot 10^6$ ), in which the boundary layer is fully turbulent. Experiments in these regimes can be challenging due to the need for large wind tunnels and wind speeds. In the context of stationary cylinders, a series of experiments have been performed at these very large Reynolds numbers (Roshko, 1961; Achenbach, 1968; Jones et al., 1969; van Nunen, 1974; Schewe, 1983). These studies generally agree well on the value of the separation angle and the location of the minimum pressure coefficient. However, large discrepancies are found between the various experimental data for the values of the aerodynamic quantities, such as pressure coefficient, lift and drag coefficients, and Strouhal number. Jones et al. (1969) also looked at a circular cylinder under forced vibration. Their study showed that a lift amplification exists and is due to the cylinder motion, in agreement with other works. Numerical studies have also been performed for flow past 2D and 3D stationary cylinders. These include Unsteady Reynolds Navier–Stokes (URANS) models (Travin et al., 2000; Catalano et al., 2003; Ong et al., 2009; Rosetti et al., 2012), large-eddy simulations (LES) (Breuer, 2000; Catalano et al., 2003; Singh and Mittal, 2005) and detached-eddy simulations (DES) (Travin et al., 2000; Squires et al., 2008). Scatter has been observed between the various URANS simulations and was attributed to either different wall function implementations or the fact that some simulations were done in 2D instead of 3D. In most cases, the numerical results also deviate from the experiments, especially with URANS. The latter methodology indeed presents shortcomings, such as an isotropic eddy viscosity, homogeneous Reynolds stresses, and the modelling of the full range of turbulent eddies (Rosetti et al., 2012). Yet, it was found that URANS can still lead to satisfactory engineering results in the supercritical flow regime (Ong et al., 2009). The present study will go a step further by presenting URANS results of a freely-vibrating cylinder in the supercritical regime ( $Re \geq 3.6 \cdot 10^6$ ). To the best of the authors' knowledge, this is the first numerical work to do so.



The paper is organised as follows. Section 2 presents the fluid-dynamics and structural-dynamics models used in this study. It also explains the algorithm used to couple these models and perform two-way coupled fluid-structure interaction (FSI) simulations of a freely-vibrating cylinder. Section 3 shows the results for two different regimes. First, laminar flow is considered in order to validate both the models and the FSI algorithm. Results of a freely-vibrating cylinder are presented and compared to the literature. Second, the turbulent supercritical regime is considered for three cases: stationary cylinder, cylinder undergoing forced vibrations, and cylinder undergoing free vibrations. Finally, conclusions are drawn in Section 4.

## 2 Computational approach

### 2.1 Fluid dynamics model

The computational fluid dynamics (CFD) model used in this study is the open-source code Open-FOAM-v1812. The model uses a finite-volume discretisation of the incompressible Navier–Stokes equations for a Newtonian fluid. In the laminar regime, these equations are solved directly, without using a turbulence model, through direct numerical simulations (DNS). In the turbulent regime, the Unsteady Reynolds-Averaged Navier–Stokes (URANS) equations are solved using a  $k$ - $\omega$  SST turbulence model (Menter, 1994), namely

$$\frac{\partial \bar{\mathbf{u}}}{\partial t} + \nabla \cdot (\bar{\mathbf{u}}\bar{\mathbf{u}}) = -\frac{\nabla \bar{p}}{\rho} + \nabla \cdot (\nu \nabla \bar{\mathbf{u}}) - \nabla \cdot (\overline{\mathbf{u}'\mathbf{u}'}), \quad (1)$$

$$\nabla \cdot \bar{\mathbf{u}} = 0, \quad (2)$$

where  $\mathbf{u}(\mathbf{x}, t) = \bar{\mathbf{u}}(\mathbf{x}, t) + \mathbf{u}'(\mathbf{x}, t)$  and  $\overline{\mathbf{u}'} = 0$ . Additionally, the turbulence model assumes that

$$-\overline{u'_i u'_j} = 2\nu_t S_{ij} - \frac{2}{3}\delta_{ij}k, \quad (3)$$

with

$$S_{ij} = \frac{1}{2} \left( \frac{\partial \bar{u}_i}{\partial x_j} + \frac{\partial \bar{u}_j}{\partial x_i} \right) - \frac{1}{3}\delta_{ij} \frac{\partial \bar{u}_k}{\partial x_k}, \quad (4)$$

and

$$k = \frac{1}{2} \overline{u'_i u'_i}. \quad (5)$$

The specific implementation of the model is that presented by Menter et al. (2003), with a revised turbulence specific dissipation rate production term from Menter and Esch (2001). The turbulent specific dissipation rate  $\omega$  is computed by solving the following equation,

$$\frac{\partial \omega}{\partial t} + \frac{\partial u_j \omega}{\partial x_j} = \gamma \frac{\tilde{P}_k}{\nu_t} - \beta \omega^2 + \frac{\partial}{\partial x_j} \left[ (\nu + \sigma_\omega \nu_t) \frac{\omega}{x_j} \right] + 2(1 - F_1) \sigma_{\omega_2} \frac{1}{\omega} \frac{\partial k}{\partial x_j} \frac{\partial \omega}{\partial x_j}, \quad (6)$$



**Table 1.** Turbulence coefficients for the present  $k$ - $\omega$  SST model.

Model coefficient	Value [-]
$\sigma_{k_1}$	0.85
$\sigma_{k_2}$	1
$\sigma_{\omega_1}$	0.5
$\sigma_{\omega_2}$	0.856
$\beta_1$	3/40
$\beta_2$	0.0828
$\gamma_1$	5/9
$\gamma_2$	0.44
$\beta^*$	0.09
$a_1$	0.31

where the blending function  $F_1$  is given by

$$85 \quad F_1 = \tanh \left[ \left[ \min \left[ \max \left( \frac{\sqrt{k}}{\beta^* \omega \gamma}, \frac{500\nu}{\gamma^2 \omega} \right), \frac{4\sigma_{\omega_2} k}{CD_{k\omega} \gamma^2} \right] \right]^4 \right], \quad (7)$$

and

$$CD_{k\omega} = \max \left( 2\sigma_{\omega_2} \frac{1}{\omega} \frac{\partial k}{\partial x_j} \frac{\partial \omega}{\partial x_j}, 10^{-10} \right). \quad (8)$$

The transport equation for the turbulent kinetic energy  $k$  is given by

$$\frac{\partial k}{\partial t} + \frac{\partial u_j k}{\partial x_j} = \tilde{P}_k - \beta^* k \omega + \frac{\partial}{\partial x_j} \left[ (\nu + \sigma_k \nu_t) \frac{k}{x_j} \right], \quad (9)$$

90 where the limited production term  $\tilde{P}_k$  is given by

$$\tilde{P}_k = \min(P_k, 10\beta^* k \omega), \quad (10)$$

and

$$P_k = \nu_t \frac{\partial u_i}{\partial x_j} \left( \frac{\partial u_i}{\partial x_j} + \frac{\partial u_j}{\partial x_i} \right). \quad (11)$$

Furthermore, the values of the turbulence coefficients are given in Tab. 1. If needed, the constants are blended (typically close  
 95 to the boundary layer) by the following interpolation,

$$\phi = F_1 \phi_1 + (1 - F_1) \phi_2, \quad (12)$$

where  $\phi$  represents any of the coefficients in Tab. 1. Once the two turbulence transport equations are solved, the eddy viscosity field is obtained as

$$\nu_t = \frac{a_1 k}{\max(a_1 \omega, \Omega F_2)}, \quad (13)$$



100 in which  $\Omega$  is the magnitude of the strain rate tensor, and  $F_2$  is the following blending function,

$$F_2 = \tanh \left[ \left[ \max \left( \frac{2\sqrt{k}}{\beta^* \omega \gamma}, \frac{500\nu}{\gamma^2 \omega} \right) \right]^2 \right]. \quad (14)$$

The equations are discretised using second-order methods in both space and time. Only the equations for  $k$  and  $\omega$  are solved using a first-order upwind scheme. The PIMPLE algorithm is used for the pressure-velocity coupling.

## 2.2 Structural dynamics model

105 The two-dimensional cylinder is modelled as a rigid body of mass  $m$  attached to a linear spring, with spring constant  $k$ , and a viscous damper, with damping coefficient  $\xi$ . The motion of the rigid body is constrained so that it cannot rotate and can only translate in the  $y$ -direction transverse to the inflow. The response of the body is therefore governed by the equations of motion of a single degree-of-freedom oscillator, i.e.

$$m\ddot{y} + c\dot{y} + k_s y = F_y, \quad (15)$$

110 where  $\ddot{y}$ ,  $\dot{y}$ , and  $y$  are the  $y$ -component of the linear acceleration, velocity and displacement, respectively, of the center of gravity of the structure and  $F_y$  is the resultant traction force exerted on the structure by the fluid. Equation (15) can be written as

$$\ddot{y} + 2\zeta\omega_n\dot{y} + \omega_n^2 y = \frac{F_y}{m}, \quad (16)$$

115 where  $\omega_n = \sqrt{k_s/m}$  is the natural frequency of the structure and  $\zeta$  is the damping coefficient defined as the ratio between the actual damping and the critical value, i.e.

$$\zeta = \frac{c}{2\sqrt{k_s m}}. \quad (17)$$

For a three-dimensional tower, the values for mass, stiffness and damping vary along the tower. Here, a modal analysis was performed to lump these values into a single value representing the two-dimensional property of the cylinder. Equation (16) is further non-dimensionalised as

$$120 \quad \ddot{y}^* + 2\zeta\dot{y}^* + y^* = (U^*)^2 \frac{C_L}{m^*}, \quad (18)$$

denoting  $y^* = y/D$  ( $D$  being the cylinder diameter),  $t^* = t/\omega_n$ , and  $m^* = 2m/(\rho D)$ . Additionally, the lift coefficient is defined as  $C_L = 2F_y/(\rho U^2 D)$  and the reduced velocity is  $U^* = U/(D\omega_n)$ .

## 2.3 Fluid-structure interaction coupling algorithm

125 In this work, fluid-structure interactions are modelled using a partitioned approach, whereby the fluid and structural dynamics are solved alternatively at every time step. Here, both weakly- and strongly- coupled schemes are considered. This is illustrated

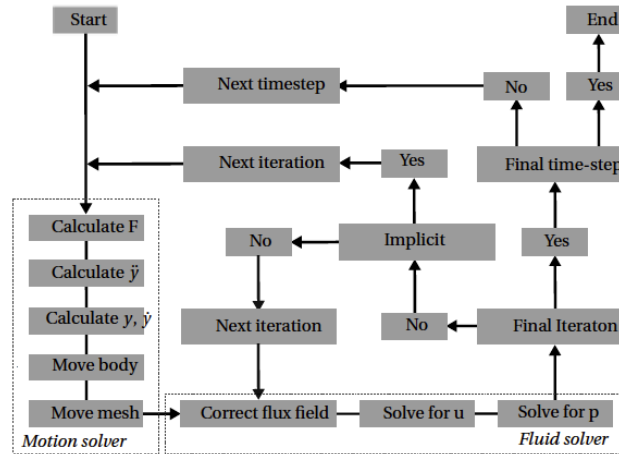


**Figure 1.** Sketch of the coupling weakly- (explicit) and strongly- (implicit) coupled algorithms between structure and fluid solvers.

by Fig. 1. At the start of a new time step, Eq. (15) is solved for the structural dynamics. Once the structure displacement is known, the geometry is moved accordingly and the mesh is diffused using a spherical linear interpolation scheme (SLERP) algorithm. With this approach, it is possible to specify a mesh region where the cells preserve their shape during motion. In this work, for the freely-vibrating cases, the mesh in a distance of up to  $25D$  around the cylinder is kept rigid throughout the simulations, in order to keep its initial high-quality characteristics in the O-grid block. By contrast, the mesh deformation is applied to all cells located further away from the cylinder. Once the mesh has moved, the fluid dynamics solver solves the Navier–Stokes equations accounting for the mesh motion using an Arbitrarily Lagrangian Eulerian approach. In the weakly-coupled algorithm, the fluid-dynamics equations are solved iteratively without solving again for the structural dynamics. As such, the structural and mesh motion are only solved once per time step. By contrast, in the strongly-coupled approach, the structural dynamics equations are solved for each sub-iteration of the fluid solver. Thus, the structural dynamics and mesh movement are solved multiple times per time step.

In this work, a weakly-coupled algorithm was found to give accurate results for modelling VIV in the laminar regime. In that case, the structural dynamics equations were also solved using an explicit solver, the so-called symplectic integrator (Dullweber et al., 1997), which is based on the leapfrog method. The explicit character of this solver leads to a constant structural displacement for each iteration within a time step, while the acceleration and velocity may change at each iteration. The structural displacement of the current time step is only dependent on the acceleration computed at the previous time step. In the turbulent regime, a strongly-coupled FSI scheme was adopted and 3 to 4 sub-iterations were necessary between fluid and structural solvers to achieve accurate results. In that case, an implicit Newmark structural solver was further used with the so-called average constant acceleration method (Newmark, 1959).

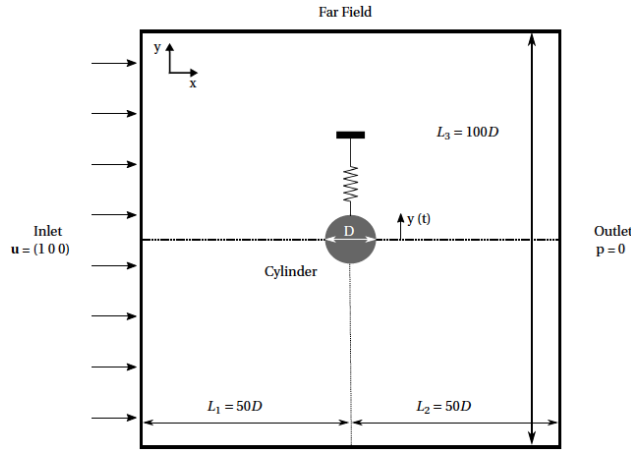


**Figure 2.** Sketch of the computational domain.

### 145 3 Results

The results are shown for two distinct flow regimes. First, a freely-vibrating cylinder is considered in a laminar flow in order to validate both the setup and the fluid-structure interaction algorithm. Second, the results are presented in a turbulent regime relevant for wind turbines. In that case, stationary cylinder, forced vibrations, and free vibrations are considered.

#### 3.1 Laminar flow

##### 150 3.1.1 Simulation setup

The computational domain used in the present work is sketched in Fig. 2. The cylinder is centered in a squared domain of length  $50D$ ,  $D$  being the cylinder diameter. A uniform streamwise velocity field is imposed as initial condition and also as a Dirichlet boundary condition at the inlet of the domain. A zero-pressure Dirichlet condition is set at the outlet. The lateral far-field boundaries are set as slip walls. In this subsection, free-vibration results are shown whereby the dynamics of the cylinder is determined by solving Eq. (15). The domain is meshed with a structured hexahedral grid, with a minimum cell height at the cylinder corresponding to  $y^+ = yu_\tau/\nu = 1$ , where  $u_\tau = \sqrt{\tau_w/\rho}$  is the friction velocity at the wall. For the present laminar flow computations, this gives a cell height at the cylinder boundary of  $\Delta y = 0.05$ . A mesh convergence analysis was performed and led to the conclusions that a mesh with 30,096 cells was sufficient to obtain accurate converged results. The time step size was further varied to keep  $CFL = 0.7$  for all the computations.

##### 160 3.1.2 Free vibration

This section shows the results of a freely-vibrating cylinder in the laminar regime and compares the results with those available in the literature (Carmo et al., 2011), where a loosely-coupled numerical FSI framework was also used. The simulations are

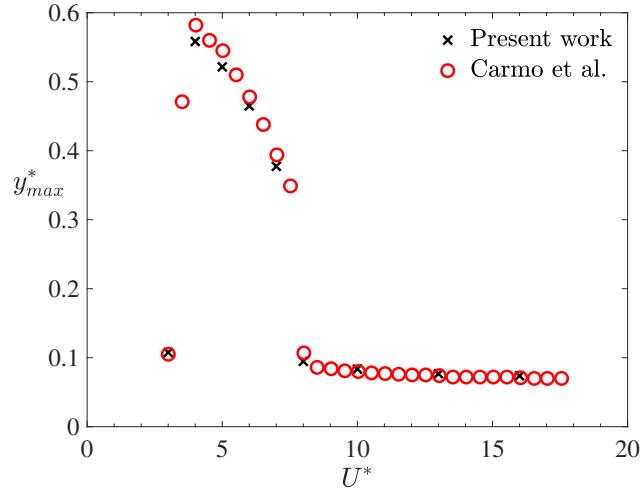


**Figure 3.** Non-dimensional maximum motion amplitude as a function of the reduced velocity for  $Re = 150$ ,  $m^* = 2$ , and  $\zeta = 0.007$ .

conducted at a Reynolds number of  $Re = 150$ , a mass ratio  $m^* = 4m/(\rho\pi D^2 L) = 2$ , and a damping factor of  $\zeta = 0.007$ . The reduced velocity  $U^* = U/(\omega_n D)$  varies in the range  $2.5 < U^* < 16$ . The non-dimensional maximum amplitude of the cylinder is shown in Fig. 3, for both the present simulations and the results from the literature. The lock-in region is clearly identified for  $4 < U^* < 7$  and good agreement between the present results and the reference solution is obtained for the whole range of reduced velocities. Figure 4 shows the cylinder frequency divided by its natural frequency. Again, good agreement is obtained between the present results and the literature. As expected, the motion frequency equals the natural frequency in the lock-in region (i.e.  $\omega/\omega_n = 1$ ), whilst the frequency ratio follows the Strouhal relation outside the lock-in band. These results demonstrate that the present weakly-coupled FSI model is capable of predicting the dynamics of a light cylinder undergoing VIV in laminar flow conditions.

### 3.2 Turbulent flow

#### 3.2.1 Simulation setup

The computational domain and boundary conditions are identical to those used in the previous subsection. However, since a turbulence model is used here, additional boundary and initial conditions are needed for the turbulent quantities. In particular, the initial value of the turbulent kinetic energy is set to

$$k_{t=0} = \frac{3}{2} (T I u_\infty)^2, \quad (19)$$



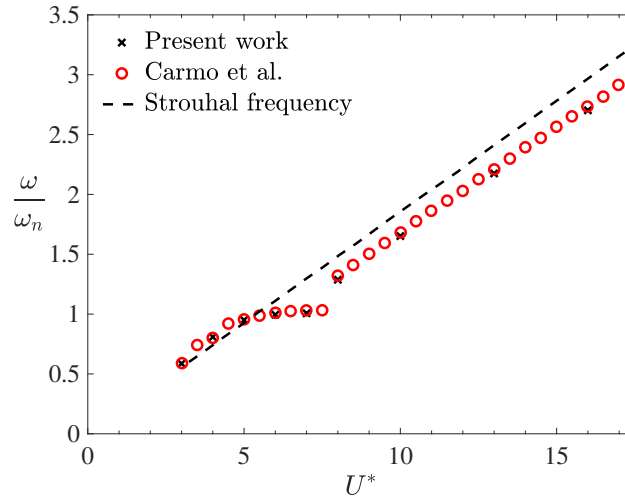


**Figure 4.** Ratio of the motion frequency to the natural frequency as a function of the reduced velocity for  $Re = 150$ ,  $m^* = 2$ , and  $\zeta = 0.007$ .

with the turbulence intensity being set at  $TI = 0.03$  and  $u_\infty = 1$ , whilst the initial value of the turbulence specific dissipation rate is equal to

$$180 \quad \omega_{t=0} = \frac{\rho k}{\mu} \left( \frac{\mu_t}{\mu} \right)^{-1}, \quad (20)$$

with  $\mu_t/\mu = 10$ . The initial value of the eddy viscosity is  $\nu_t = 0$ . Regarding the boundary conditions, Dirichlet conditions are imposed on both  $k$  and  $\omega$  at the inlet, with values equal to the initial ones, respectively, and Neumann conditions are imposed at the outlet. At the cylinder, the mesh is fine enough to resolve the flow up to the viscous sublayer ( $y^+ = 1$ ) using prism layers around the cylinder, with a mesh growth ratio equal to 1.2 and a minimum cell height at the cylinder equal to  $\Delta y = 7 \cdot 10^{-6}$ .

185 Converged results were obtained for a mesh with 98,730 grid points. As for the laminar flow simulations, the maximum CFL number was kept constant at  $CFL = 0.7$ . Since the viscous sublayer is mostly laminar, the turbulent quantities are such that turbulence is suppressed at the wall. Thus, at the cylinder boundary,  $k = 10^{-10} m^2/s^2$ ,  $\nu_t = 0$ , and

$$\omega = \frac{6\mu}{\beta_1 y_{wall}^2}, \quad (21)$$

with  $\beta_1 = 0.075$  (Menter, 1992).

### 190 3.2.2 Flow past a stationary cylinder

Before considering flow past moving cylinders, the accuracy of the  $k - \omega$  SST turbulence model in the supercritical regime is first assessed on flow past a stationary cylinder at a Reynolds number  $Re = 3.6 \cdot 10^6$ . Table 2 compares the results of the present simulations with numerical and experimental data from the literature, in terms of Strouhal number  $St$ , mean drag coefficient  $C_{D,mean}$ , base pressure coefficient  $c_{p,b}$  at  $\theta = 180^\circ$ , and flow separation angle  $\theta_{sep}$ . The values marked with a double asterisk  
 195 are estimated indirectly based on the available pressure distribution where the constant pressure plateau is reached. Overall, it



**Table 2.** Comparison of data for flow past a stationary cylinder in the supercritical regime.

Data	$Re$	$St$	$C_{D,mean}$	$c_{p,b}$	$\theta_{sep}$ ( $^{\circ}$ )
Present work	$3.6 \cdot 10^6$	0.32	0.42	-0.5	111
2D k- $\epsilon$ URANS (Ong et al., 2009)	$3.6 \cdot 10^6$	0.31	0.46	$\approx -0.54^{**}$	114
DES (Travin et al., 2000)	$3 \cdot 10^6$	0.35	0.41	-0.53	111
Experimental (Achenbach, 1968)	$3.6 \cdot 10^6$	0.25	0.76	$\approx -0.81^{**}$	115
Experimental (Jones et al., 1969)	$3.5 \cdot 10^6$	0.24	0.58	$\approx -0.65^{**}$	$\approx 125^{**}$

is observed that the present results agree well with the literature, and especially when compared with other numerical results obtained with either URANS (Ong et al., 2009) or DES (Travin et al., 2000) turbulence models. The pressure coefficient at the cylinder surface is further plotted in Fig. 5. Again, it is clear that the present URANS results match well the results from other numerical studies. Compared to experimental works (Achenbach, 1968; Jones et al., 1969), the present pressure coefficient agrees well in the front part of the cylinder, for  $0^{\circ} \leq \theta \leq 63^{\circ}$ . For larger values of  $\theta$ , the numerical results show both an earlier pressure recovery (at around  $\theta \approx 80^{\circ}$ ) and a less pronounced negative peak for  $c_p$ . It was shown by Achenbach (1968) that the transition point of the boundary layer is at  $\theta = 65^{\circ}$  for that Reynolds number. It seems that the pressure distribution starts to deviate around this point, which could indicate that the transition has an impact on the pressure distribution. The boundary layer in the experiment of Jones et al. (1969) continues to decelerate further aft (at  $\theta = 90^{\circ}$ ), which explains why the separation also occurs later in their measurements. This might indicate that the numerical models do not fully predict the detached flow accurately. This in line with previous observations made in the literature, although at different Reynolds numbers (Ferrand et al., 2006; Catalano et al., 2003). The friction coefficient at the cylinder surface is also plotted in Fig. 6. The present numerical results agree well with other numerical studies that use either LES (Catalano et al., 2003) or DES (Travin et al., 2000). The peak of maximum friction coefficient slightly underestimates the other numerical studies. However, the overall agreement is good and the separation location is also accurately captured and compares well with the experiment of Achenbach (1968). The numerical values of  $c_f$  for  $0^{\circ} \leq \theta \leq 90^{\circ}$  are generally much higher than the experimental values. This can be explained by the fact that the numerical studies assume fully turbulent transition, and therefore, lead to significantly higher values of friction coefficient. In particular, the over-prediction is caused by the fact that the laminar flow at the beginning part of the cylinder wall is not taken into account in the numerical models. This is in line with the observations of Travin et al. (2000) and Catalano et al. (2003). Only the URANS simulations of Ong et al. (2009) show much smaller values of friction coefficient. However, this study used a  $k - \epsilon$  turbulence model, which is known to perform poorly with flow separation and strong pressure gradients. This could explain why these URANS results under-predict the skin-friction coefficient compared to the other numerical studies. Despite the discrepancies in  $c_p$  and  $c_f$  between numerical and experimental results, the present turbulence model is deemed to be adequate for the purpose of this work as it provides results that are in line with other trustful numerical studies in the supercritical regime.

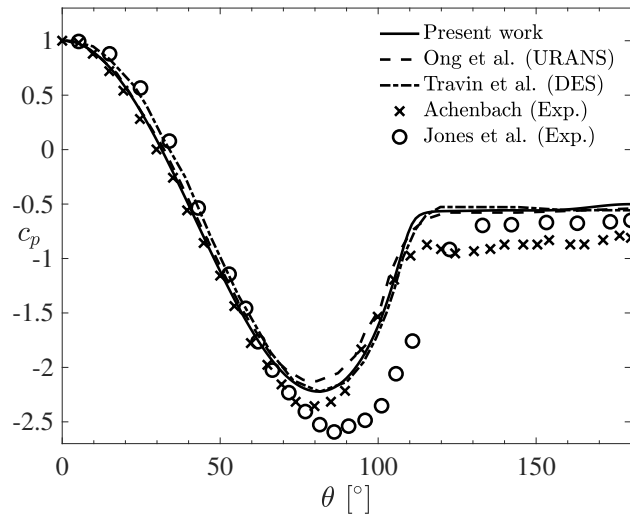


**Figure 5.** Time-averaged pressure distribution for flow past a stationary cylinder in the supercritical turbulent regime.

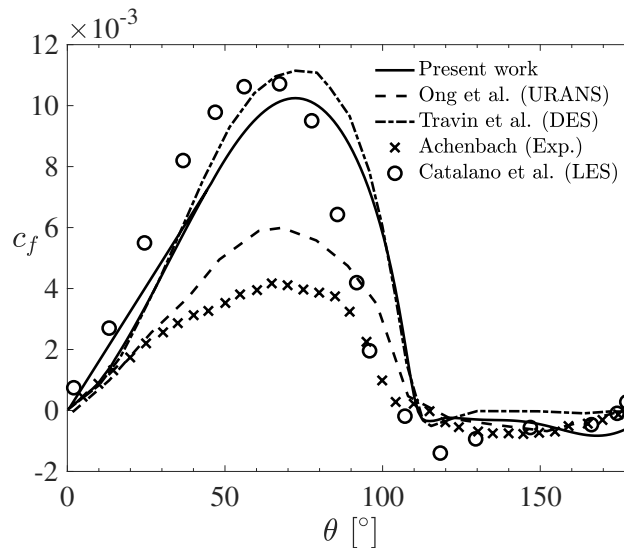


**Figure 6.** Time-averaged friction coefficient for flow past a stationary cylinder in the supercritical turbulent regime.

### 3.2.3 Flow past a cylinder under forced vibration

In this section, the transverse motion of the cylinder is prescribed for different values of Reynolds number, and hence frequency ratio. The frequency ratio is defined as  $\omega^* = \omega_n / \omega_{(\text{shed, stat})}$ , where  $\omega_n$  is the natural frequency of the cylinder and  $\omega_{(\text{shed, stat})}$  is the vortex shedding frequency associated with flow past a stationary cylinder at the same Reynolds number. The latter was obtained numerically with the same mesh as for the corresponding moving cases. Seven values of the frequency ratios are



**Table 3.** Range of reduced frequencies and velocities considered for the forced vibration of a cylinder in the supercritical regime.

$\omega^*$	$U^*$	$Re$
0.58	2.524	$3.8 \cdot 10^6$
0.74	2.869	$4.3 \cdot 10^6$
0.89	3	$4.5 \cdot 10^6$
0.95	3.223	$4.8 \cdot 10^6$
1.01	3.384	$5 \cdot 10^6$
1.07	4	$6 \cdot 10^6$
1.23	5	$7 \cdot 10^6$

considered, each corresponding to a different reduced velocity and Reynolds number, as indicated in Table 3. The simulations are further ran for seven different values of the prescribed maximum motion amplitude. The root-mean-square of the lift coefficient (non-dimensionalised by its value for a stationary cylinder) is shown in Fig. 7, for different frequency ratios  $\omega^*$  and prescribed motion amplitudes  $y_{max}^*$ . As expected, the lift magnification due to the cylinder motion increases with both  $\omega^*$  and  $y_{max}^*$ . The increase with  $\omega^*$  is rather linear, except close to  $\omega^* = 1$ . The peak in lift magnification around a unitary reduced frequency is believed to be a consequence of the wake lock-in on the cylinder motion. For  $\omega^* > 1$  and  $y_{max}^* \geq 1$ , our simulation results indicate that the lift magnification becomes very large, which is believed to be due to the effective added mass of the fluid caused by the vorticity dynamics (Williamson and Govardhan, 2008).

Another observation is that the lock-in band width increases with increasing motion amplitudes, with a move towards lower reduced frequencies as the oscillation amplitude increases. Both these observations, namely increased lift magnification at high frequency ratios and wider lock-in band at larger motions, were observed in the experimental results obtained from NASA under similar conditions (Jones et al., 1969), as shown in Fig. 8. Although the experimental results show some scatter, a peak of lift magnification is obtained around  $\omega^* = 1$ , decreasing for slightly larger values of  $\omega^*$ , before increasing further as  $\omega^* > 1$  (see for example the results at  $y_{max}^* = 0.0278$  in Fig. 8).

Although the cylinder motion is prescribed, it is interesting to look in more details at the feedback mechanism between the cylinder and the fluid motions. In order to do this, the aerodynamic damping is analysed. It is defined as the part of the harmonic lift force that is in phase with the cylinder velocity. There are different ways to compute this damping. Here, an approach based on the time-averaged energy transfer between fluid and vibrating cylinder is considered (Bourguet et al., 2011; Gopalakrishnan, 1993), as it is believed to be accurate when signals exhibit multiple frequencies. This leads to the following expression for the aerodynamic damping,

$$C_{L,V} = -\sqrt{2} \frac{\overline{C'_L \dot{y}'}}{\sqrt{\overline{\dot{y}'^2}}}, \quad (22)$$

where  $C_L$  denotes the lift coefficient,  $q'$  is the fluctuating part of a quantity  $q$ , and  $\bar{q}$  is its time average. The aerodynamic damping is plotted for the different simulation cases in Fig. 9. For  $\omega^* \geq 1$ , it is observed that  $C_{L,V}$  increases with the motion

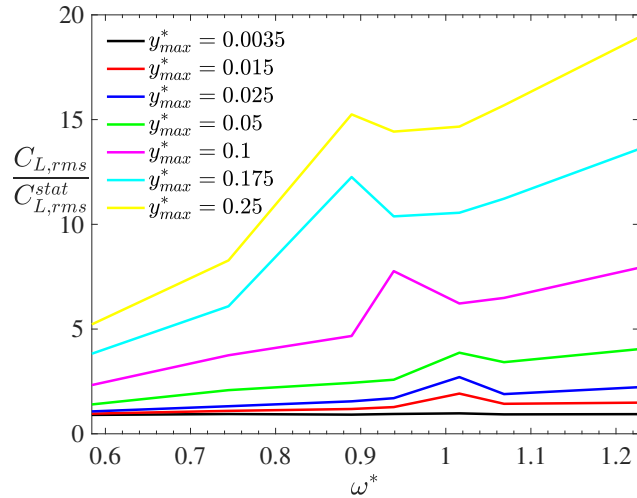


**Figure 7.** Root-mean-square of the lift coefficient (non-dimensionalised by its value for a stationary cylinder) for forced vibrations in the supercritical turbulent regime with different frequency ratios  $\omega^*$  and prescribed motion amplitudes  $y_{max}^*$ .

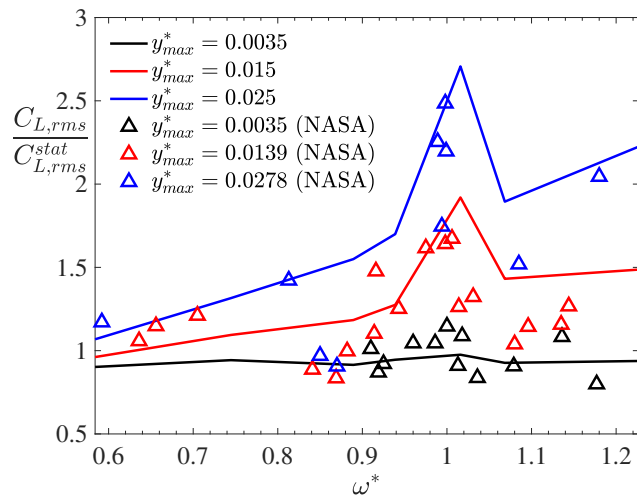


**Figure 8.** Root-mean-square of the lift coefficient (non-dimensionalised by its value for a stationary cylinder) for forced vibrations compared with NASA experimental data (Jones et al., 1969) at three values of the prescribed motion amplitude.

amplitude. This indicates that the wake dynamics tends to oppose the cylinder motion as the latter increases, hence stabilising  
 250 the system. By contrast, for  $\omega^* \leq 0.75$ , the aerodynamic damping is negative with an absolute value increasing as the cylinder  
 displacement increases. In that case, the wake dynamics tends to further amplify the system motion, hence leading to an  
 unstable system behaviour. In the lock-in band, for  $0.8 \leq \omega^* \leq 1$ , the nature of the interaction between fluid and structural  
 motion depends on the amplitude of the prescribed motion. However, a stabilising fluid-structure interaction behaviour is  
 observed for large motion amplitudes. These observations agree with that obtained from Jones et al. (1969). In particular, the

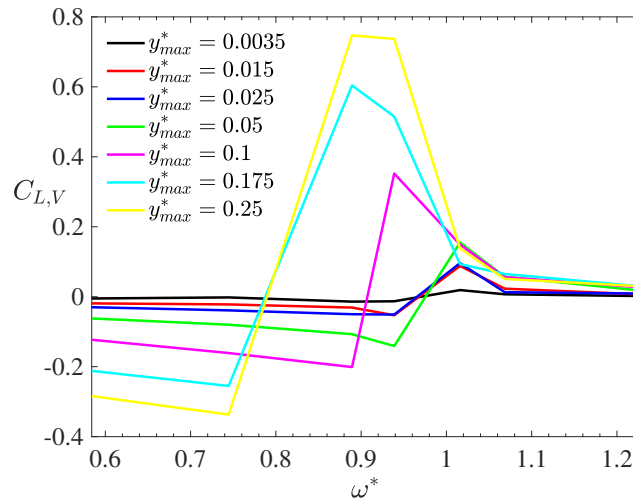


**Figure 9.** Aerodynamic damping for forced vibrations in the supercritical turbulent regime with different frequency ratios  $\omega^*$  and prescribed motion amplitudes  $y_{max}^*$ .

255 overall behaviour of the experimental aerodynamic damping in the supercritical turbulent regime, for varying frequency ratios, was found to be similar to the present CFD results.

### 3.2.4 Flow past a freely-vibrating cylinder

In this section, the cylinder is left to freely vibrate under the vortex-induced vibrations. The results are shown for a baseline value of mass ratio  $m^* = 29.6$  and damping coefficient  $\zeta = 0.003$ , which are representative of a realistic wind turbine tower.

260 The effect of these values on the results is also briefly discussed in this section. The reduced velocity is varied from  $U^* = 1.88$  to  $U^* = 10.74$ , corresponding to Reynolds numbers between  $Re = 2.8 \cdot 10^6$  and  $Re = 1.6 \cdot 10^7$ , respectively. The associated non-dimensional maximum motion amplitude under these conditions is shown in Fig. 10, in which the lock-in band can be clearly visualised. Additionally, the insets show the time evolution of the lift coefficient on the cylinder for certain values of reduced velocity. The associated values of reduced frequency,  $\omega^* = \omega_n / \omega_{(shed, stat)}$ , are also shown for each inset. These insets

265 illustrate that for some values of  $U^*$ , a non-harmonic lift response (and consequently also motion response) is obtained. Outside the lock-in region, at low values of  $U^*$ , the vortex shedding frequency is dominated by the stationary Strouhal relation and is very different from the natural frequency of the cylinder. This is also apparent from Fig. 11. In that case, the mean aerodynamic forces are similar to those of a stationary cylinder and little cylinder motion is observed. When  $U^*$  increases to values close to the lock-in band, the time histories of the aerodynamic forces and cylinder motion change. First, the cylinder displacement

270 increases substantially because the vortex shedding frequency gets closer to the natural frequency of the cylinder. Second, the cylinder motion shows two main frequency responses instead of one. The dominant frequency in the time evolutions of the lift and motion amplitude still equals the Strouhal frequency. However, performing a power spectral density on these time signals shows that a second (much smaller) frequency peak coincides with the natural frequency. This explains the observed

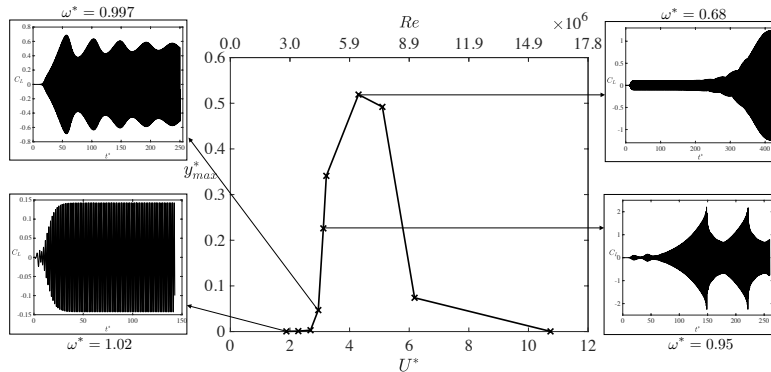


**Figure 10.** Non-dimensional maximum motion amplitude as a function of the reduced velocity for  $m^* = 29.6$ ,  $\zeta = 0.003$  and  $1.88 \leq U^* \leq 10.74$ . Insets show the time evolution of the lift coefficient at certain values of reduced velocities.

increase in cylinder motion compared to cases at smaller reduced velocities. When  $U^*$  is increased further, inside the lock-in  
 275 band, the time histories of the lift and displacement also show two frequencies. However, the dominant peak corresponds to the  
 natural frequency of the cylinder, hence confirming that the wake behaviour becomes driven by the cylinder oscillations rather  
 than the Strouhal relation. Furthermore, the lift force (and also motion displacement) alternate between growth and decay,  
 which also corresponds to a change in sign of the aerodynamic damping. In particular, when the lift force increases, the fluid  
 dynamics excites the cylinder. By contrast, when the lift force decreases, the fluid dynamics damps the cylinder motion. As  
 280 such, the vortex-induced vibrations continuously alternate between self-exciting and self-limiting behaviours. This alternation  
 of behaviours is influenced by both the mass ratio and the damping factor. If the mass ratio is reduced, the non-dimensional  
 displacement amplitude increases. This is expected as a lower mass ratio leads to a lower structural inertia when compared to  
 the fluid inertia. This makes the cylinder more susceptible to oscillations, and possibly lock-in. By contrast, for very large mass  
 ratios, the cylinder motion decreases and eventually tends to a stationary cylinder. There is thus a critical value of the mass ratio  
 285 at which the system stops undergoing enhanced fluid-structure interactions. Non-harmonic behaviours of the lift and motion  
 displacement are also less likely to occur at large mass ratios and large damping factors because the larger structural inertia  
 prevents the cylinder from changing to a different dynamic state. When  $U^*$  is increased further, in a certain range, the lift  
 force, drag force and transverse displacement do not show a clear converged pattern (see inset in Fig. 10 at  $U^* = 4.3$ ). It is not  
 excluded that, if the simulation was run for even longer times, a self-limiting behaviour could appear. However, the observed  
 290 behaviour is believed to have physical causes, rather than being a numerical artifact. This is because the operation points for  
 which this happens correspond to reduced frequencies between  $0.5 \leq \omega^* \leq 0.7$ , for which the results of the forced-vibration  
 cases led to unstable behaviours. By contrast, at smaller values of  $U^*$ , the reduced frequencies are large ( $0.9 \leq \omega^* \leq 1.2$ ) and a  
 stable forced-vibration behaviour was obtained. It is also worth noting that the large lock-in band observed in the present study  
 is in line with previous observations made in the literature at similar conditions. For example, Guilmineau and Queutey (2004)  
 295 and Assi (2009) showed large values of non-dimensional displacement for reduced frequencies as low as  $\omega^* = 0.7$ , whilst the  
 wind tunnel experiment of Feng (1968) also showed a lock-in region extending to a frequency ratio of  $\omega^* = 0.6$ .

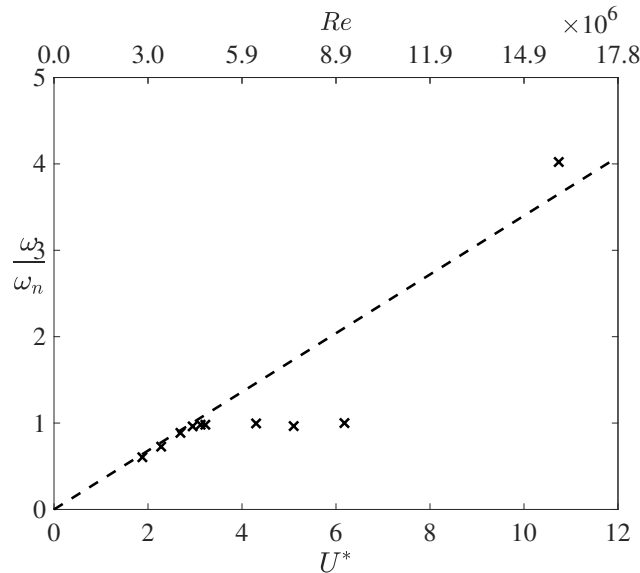


**Figure 11.** Ratio of the motion frequency to the natural frequency as a function of the reduced velocity for  $m^* = 29.6$ ,  $\zeta = 0.003$  and  $1.88 \leq U^* \leq 10.74$ .

#### 4 Conclusions

In this work, numerical simulations were performed of a two-dimensional cylinder undergoing vortex-induced vibrations. First, the fluid-structure interaction methodology was validated in the laminar regime, for which direct numerical simulations (DNS) were able to reproduce results from the literature. Second, supercritical turbulent regimes experienced by wind turbine towers were simulated using the  $k - \omega$  SST unsteady Reynolds-Averaged Navier–Stokes (URANS) model. The ability of our model to simulate flow past a stationary cylinder in the turbulent supercritical regime was demonstrated by comparing the present results with other URANS, large-eddy simulations (LES), detached-eddy simulations (DES) and experimental results from the literature. Additionally, the present tools were capable of simulating the dynamic behaviour of the cylinder (including lock-in) for a range of reduced velocities and Reynolds numbers. In particular, good agreement was found between the present results and those obtained from wind tunnel experiments under forced vibrations. When the cylinder was left free to oscillate under the effect of vortex shedding, the results highlighted a complex interplay between structural and fluid dynamics for values of reduced velocity close, or inside, the lock-in band. In particular, there was a continuous alternation between self-exciting and self-limiting vortex-induced vibrations. The physical feasibility of this interplay was supported by both the role of the aerodynamic damping, which was shown to continuously change sign at these operating points, and the results from forced-vibration oscillations under similar conditions. Future work will focus on gaining more insights into these behaviours through three-dimensional simulations of wind turbine towers undergoing VIV.





*Acknowledgements.* Viré acknowledges support from the European Commission under the H2020 project TWIND (grant agreement no. 857631) and Folkersma is supported by the H2020 ITN project AWESCO (grant agreement no. 642682) funded by the European Union's  
315 Horizon 2020 research and innovation programme under the Marie Skłodowska-Curie scheme.



## References

- Achenbach, E.: Distribution of local pressure and skin friction around a circular cylinder in cross-flow up to  $Re = 5 \times 10^6$ , *J. Fluid Mech.*, 34, 625–639, 1968.
- Assi, G.: Mechanisms for flow-induced vibration of interfering bluff bodies, Ph.D. thesis, Imperial College London, 2009.
- 320 Belloli, M., Giappino, S., Muggiasca, S., and Zasso, A.: Force and wake analysis on a single circular cylinder subjected to vortex induced vibrations at high mass ratio and high Reynolds number, *J. Wind Eng. Ind. Aerodyn.*, 103, 96–106, 2012.
- Bourguet, R., Karniadakis, G., and Triantafyllou, M.: Lock-in of the vortex-induced vibrations of a long tensioned beam in shear flow, *J. Fluids and Structures*, 27, 838–847, 2011.
- Breuer, M.: A challenging test case for large eddy simulation: high Reynolds number circular cylinder flow, *Int. J. Heat Fluid Flow*, 21, 325 648–654, 2000.
- Brika, D. and Laneville, A.: Vortex induced vibrations of a long flexible circular cylinder, *J. Fluid Mech.*, 320, 117–137, 1993.
- Carmo, B., Sherwin, S., Bearman, P., and Willden, R.: Flow-induced vibration of a circular cylinder subjected to wake interference at low Reynolds number, *J. Fluids and Structures*, 27, 503–522, 2011.
- Catalano, P., Wang, M., Iaccarino, G., and Moin, P.: Numerical simulation of the flow around a circular cylinder at high Reynolds numbers, 330 *Int. J. Heat Fluid Flow*, 24, 463–469, 2003.
- Derksen, A.: Numerical simulation of a forced and freely-vibrating cylinder at supercritical Reynolds numbers, Master’s thesis, TU Delft and Siemens, 2019.
- Dullweber, A., Leimkuhler, B., and McLachlan, R.: Symplectic splitting methods for rigid body molecular dynamics, *Journal of Chemical Physics*, 107, 5840–5851, 1997.
- 335 Feng, C.: The measurement of vortex-induced effects in flow past stationary and oscillating circular D-section cylinders, Ph.D. thesis, The University of British Columbia, 1968.
- Ferrand, P., Boudet, J., Caro, J., Aubert, S., and Rambeau, C.: Unsteady Aerodynamics, Aeroacoustics and Aeroelasticity of Turbomachines, chap. Analyses of URANS and LES capabilities to predict vortex shedding for rods and turbines, pp. 381–392, Springer, 2006.
- Gopalakrishnan, R.: Vortex-induced forces on oscillating bluff cylinders, Ph.D. thesis, Massachusetts Institute of Technology, 1993.
- 340 Govardghan, C. and Williamson, C.: Modes of vortex formation and frequency response of a freely vibrating cylinder, *J. Fluid Mech.*, 420, 85–130, 2000.
- Govardghan, C. and Williamson, C.: Defining the ‘modified Griffin plot’ in vortex-induced vibrations: revealing the effect of Reynolds number using controlled damping, *J. Fluid Mech.*, 560, 147–180, 2006.
- Griffin, O.: Vortex-excited cross-flow vibrations of a single cylindrical tube, *ASME Journal Pressure Vessel Technology*, 102, 158–166, 1980.
- 345 Guilmineau, E. and Queutey, P.: Numerical simulation of vortex-induced vibration of a circular cylinder with low mass-damping in a turbulent flow, *J. Fluids and Structures*, 19, 449–466, 2004.
- Heinz, J., Sorensen, N., Zahle, F., and Skrzypinski, W.: Vortex-induced vibrations on a modern wind turbine blade, *Wind Energy*, 19, 2041–2051, 2016.
- Horcas, S., Madsen, M., Sorensen, N., and Zahle, F.: Recent advances in CFD for wind and tidal offshore turbines, chap. Suppressing vortex 350 induced vibrations of wind turbine blades with flaps, Springer, 2019.
- Jones, G., Cincotta, J., and Walker, R.: Aerodynamic Forces on a Stationary and Oscillating Circular Cylinder at High Reynolds Numbers, Technical report TR R-300, NASA, 1969.



- Livanos, D.: Investigation of Vortex Induced Vibrations on Wind Turbine Towers, Master's thesis, TU Delft and Siemens, 2018.
- Menter, F.: Improved two-equation k- $\omega$  turbulence models for aerodynamic flows, Technical Memorandum 103978, NASA, 1992.
- 355 Menter, F.: Two-equation eddy-viscosity turbulence models for engineering applications, *AIAA J.*, 32, 1598–1605, 1994.
- Menter, F. and Esch, T.: Elements of industrial heat transfer prediction, in: *Proceedings of the 16th Brazilian Congress of Mechanical Engineering (COBEM)*, pp. 117–127, 2001.
- Menter, F., Kuntz, M., and Langtry, R.: Ten Years of Industrial Experience with the SST Turbulence Model, in: *The Fourth International Symposium on Turbulence, Heat and Mass Transfer*, vol. 4, pp. 625–632, 2003.
- 360 Newmark, N.: A method of computation for structural dynamics, *Journal of Engineering Mechanics*, 85, 67–94, 1959.
- Ong, M., Utnes, T., Holmedal, L., Myrhaug, D., and Pettersen, B.: Numerical simulation of flow around a smooth circular cylinder at very high Reynolds numbers, *Marine Structures*, 22, 142–153, 2009.
- Rosetti, G., Vaz, G., and Fajarra, A.: URANS Calculations for Smooth Circular Cylinder Flow in a Wide Range of Reynolds Numbers: Solution Verification and Validation, *J. Fluids Engineering*, 134, 1–18, 2012.
- 365 Roshko, A.: Experiments on the flow past a circular cylinder at very high Reynolds number, *J. Fluid Mech.*, 10, 345–356, 1961.
- Schewe, G.: On the force fluctuations acting on a circular cylinder in crossflow from subcritical up to transcritical Reynolds numbers, *J. Fluid Mech.*, 133, 265–285, 1983.
- Singh, S. and Mittal, S.: Flow past a cylinder: shear layer instability and drag crisis, *Int. J. Numer. Meth. Fluids*, 47, 75–98, 2005.
- Squires, K., Krishnan, V., and Forsythe, J.: Prediction of the flow over a circular cylinder at high Reynolds number using detached-eddy simulation, *J. Wind Eng. Ind. Aerodyn.*, 96, 1528–1536, 2008.
- 370 Travin, A., Shur, M., Strelets, M., and Spalart, P.: Detached-Eddy Simulations Past a Circular Cylinder, *Flow, Turbulence and Combustion*, 63, 293–313, 2000.
- van Nunen, J.: Pressure and forces on a circular cylinder in a cross flow at high Reynolds numbers, *Flow Induced Structural Vibrations*, pp. 748–754, 1974.
- 375 Williamson, C. and Govardhan, R.: A brief review of recent results in vortex-induced vibrations, *Journal of Wind Engineering & Industrial Aerodynamics*, 96, 713–735, 2008.